

Experimental study of initial condition dependence on Richtmyer-Meshkov instability in the presence of reshock

S. Balasubramanian, G. C. Orlicz, K. P. Prestridge,^{a)} and B. J. Balakumar
*Extreme Fluids Team, P-23, Physics Division, Los Alamos National Laboratory, Los Alamos,
 New Mexico 87545, USA*

(Received 22 August 2011; accepted 15 February 2012; published online 14 March 2012)

We present an experimental study on the dependence of initial condition parameters, namely, the amplitude δ and wavenumber κ ($\kappa = 2\pi/\lambda$, where λ is the wavelength) of perturbations, on turbulence and mixing in shock-accelerated Richtmyer-Meshkov (R-M) unstable fluid layers. A single mode, membrane-free varicose heavy gas curtain (air-SF₆-air) at a shock Mach number $M = 1.2$ was used in our experiments. The density (concentration) and velocity fields for this initial configuration were measured using planar laser-induced fluorescence (PLIF) and particle image velocimetry (PIV). In order to understand the effects of multi-mode initial conditions on shock-accelerated mixing, the evolving fluid interface formed during the incident shock ($M = 1.2$) was shocked again by a reflected shock wave at various times using a movable wall, thus enabling us to change both δ and κ simultaneously. A dimensionless length-scale defined as $\eta = \kappa\delta$ is proposed to parametrically link the initial condition dependence to late-time mixing. It was observed experimentally that high wavenumber (short wavelength) modes enhance the mixing and transition to turbulence in these flows. Statistics such as power spectral density, density self-correlation, turbulent kinetic energy, and the *rms* of velocity fluctuations were measured using simultaneous PLIF-PIV to quantify the amount of mixing for varying values of η . The results indicate a dependence of initial condition parameters on mixing at late times. The results of this study present an opportunity to predict and “design” late-time turbulent mixing that has applications in inertial confinement fusion and general fluid mixing processes.
 © 2012 American Institute of Physics. [<http://dx.doi.org/10.1063/1.3693152>]

I. INTRODUCTION

The effects of initial conditions on turbulent mixing in shock-accelerated flows are addressed experimentally and compared with theory. The Richtmyer-Meshkov (R-M) instability arises when a density interface is impulsively accelerated by a shock wave resulting in the deposition of baroclinic vorticity ($\nabla p \times \nabla \rho$).^{1,2} Usually, the density interface consists of random perturbations (e.g., surface roughness, machining grooves inaccuracies, uneven fluid interface, etc.) which initially grow linearly before nonlinear effects emerge. At later stages, there is material mixing and an eventual transition to turbulence. The study of R-M instability is important for understanding of the inertial confinement fusion process, where a spherical capsule containing solid deuterium-tritium (DT) and an inner space filled with gaseous DT is compressed using powerful lasers.³ The imploding shock moving towards the center of the spherical shell induces the R-M instability on its inner surface due to the large density difference between the solid and gaseous DT, resulting in a rapid growth of initially present random perturbations. This rapid R-M instability development induces mixing of the ablative material of the

^{a)}Electronic mail: kpp@lanl.gov. URL: <http://www.lanl.gov/projects/shocktube/>.

shell with the gaseous DT, reducing its ability to efficiently ignite the fuel mixture.⁴ It is important to design and control these perturbations in such a way that the yield and the energy production are optimized. Other applications of this work include astrophysical phenomena, from supernovae to the dynamics of interstellar media, combustion processes, and mixing in scramjet engines (where the R-M instability has a reverse effect, in the sense that mixing of fuel and air is indispensable for effective combustion).

Turbulent mixing induced by buoyancy-driven hydrodynamic instabilities has a number of distinct features, compared with classical turbulent flows, that make theoretical and experimental modeling of such flows extremely challenging. Anisotropy and inhomogeneities arise due to various factors ranging from initial condition variations, presence of shocks, material discontinuities, and associated baroclinic effects. It has been thought that both Rayleigh-Taylor (R-T) and R-M turbulence reach an isotropic state at late times and the flow becomes independent of the initial perturbations and is controlled only by the local small-scales present in the flow.^{5,6} However, recently there is a growing body of fundamental research that indicates only special turbulent flows are truly self-similar,⁷⁻¹⁶ thus bringing forth the issue of memory of initial conditions on late-time flow development. An interesting observation from the theoretical and numerical studies for R-T instability⁸⁻¹⁰ and R-M instability¹¹⁻¹⁷ has shown that carefully imposed initial conditions can affect the rate of mixing, and that the turbulence does not reach a unique self-similar state. It is necessary to obtain experimental evidence in order to validate these numerical results. The extreme conditions under which this process occurs makes experimental observation a challenging task, and there are only a handful of experimental results that indicate an initial condition dependence on late-time R-M mixing. Experiments in air and SF₆ done by Prasad *et al.*¹⁸ examined the influence of initial conditions on the late-time growth of the turbulent mixing zone (TMZ). The initial conditions were taken as a series of large-scale sinusoidal perturbations, broken by a high wavenumber component introduced through a wire mesh. It was concluded that there is a weak dependence of initial conditions on mixing, with the largest wavelengths producing the thickest mixing layer. However, for experiments with mesh/membranes, it is difficult to understand the added effects of the mesh on the R-M instability, and measurements in these experiments are impaired by contamination of the flow with small pieces of wire/diaphragms that are left behind after the passage of the shock wave. The most recent work by Balakumar *et al.*^{19,20} involved study of various initial condition configurations on mixing with and without reshock. In this study the initial conditions were formed using a membraneless gas curtain which is R-M unstable.¹⁹ This study revealed that starting with different initial configurations led to different development in mixing after reshock without a self-similar state of mixing. In experiments reported by Jacobs and Sheeley,²¹ a liquid interface was used to study the effects of varying initial interface configuration on incompressible R-M instability growth. It was shown that the late-time growth curves of many different experiments seem to collapse to a single curve when correlated with the circulation deposited by the impulsive acceleration, and a theory for modeling the late-time evolution of the instability using a row of vortices was developed. Most of the experimental work on R-M instability and mixing has focused on the effect of single-mode initial conditions on the growth of the TMZ with shock and reshock.^{13,22} In experiments with reshock, the observed linear growth persists for the same amount of time, as for first shock. The disparities in mixing that are seen are explained by the fact that the turbulence is re-energized during reshock by shock interaction with perturbations grown by the first shock process. Despite these studies, the effect of initial conditions on the late-time R-M mixing and turbulence is still unclear. In this present work, we experimentally study the multi-mode initial condition effects on late-time mixing in a R-M unstable fluid layer after reshock, by looking at various mixing and turbulence statistics. Such a study is important since the efficacy of species mixing occurring in shock-accelerated flows is influenced by the dynamics of the turbulence contained within the flow, which are, in turn, thought to be dependent on initial configurations. The experimental results from this study will be helpful in understanding how to initialize numerical simulations, and in improving our methods for modeling unsteady, turbulent flows. In Sec. II, our experimental set up and initial conditions are presented. Section III describes the results of the reshock experiments on multi-mode initial conditions followed by discussion. The conclusions from this study are summarized in Sec. IV.

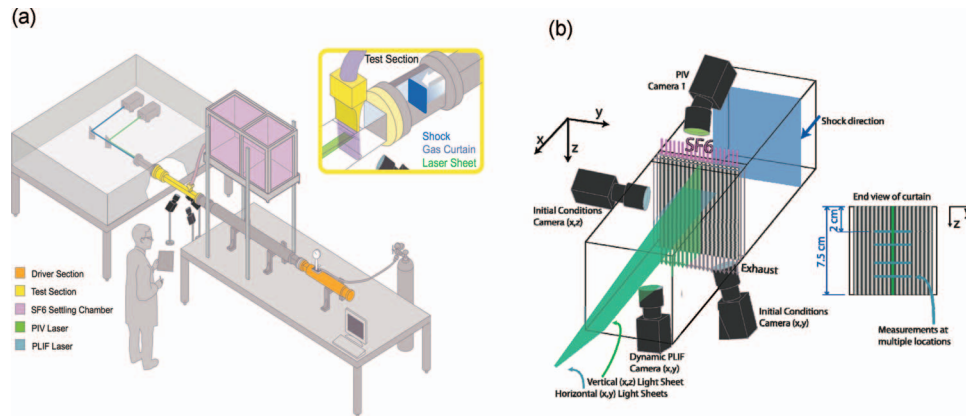


FIG. 1. (a) Schematic of the Gas Shock Tube facility, (b) illustration of the PIV and PLIF diagnostics to measure the initial conditions and evolution of R-M instability.

II. EXPERIMENTAL SETUP AND INITIAL CONDITIONS

The experiments were carried out at the Los Alamos Horizontal Gas Shock Tube facility shown in Figure 1(a).²⁰ A Mach $M = 1.2$ shock wave is generated using nitrogen as the driver gas and air as the driven gas, within a 75×75 mm square cross section tube with a total length of approximately 5.4 m. The shock wave travels a streamwise distance of $x \approx 3.3$ m before entering a 45 cm long test section. This new, longer test section allows us to study the R-M instability evolution and turbulent mixing after shock interaction at later times than previously in this facility. To form the gas curtain, a mixture of SF_6 and acetone is flowed into a settling chamber as illustrated by the SF_6 settling chamber in Figure 1(a). Membraneless initial conditions in the form of a varicose gas curtain flow from this settling chamber into the test section using a nozzle whose primary amplitude and wavelength of perturbations is $\delta_0 = 3$ mm and $\lambda_0 = 3.6$ mm. The diffusive and convective processes together act to create a layer containing varicose perturbations on either edge. The Atwood number defined as $A = \frac{(\rho_2 - \rho_1)}{(\rho_2 + \rho_1)}$ for this study is $A = 0.57$ at the centerline of the gas curtain taken at a plane $z = 20$ mm below the nozzle exit. The generated shock wave impinges upon the curtain of SF_6 flowing through the nozzle. The heavy gas exits the test section through an exit plenum attached to the bottom wall of the shock tube, that is maintained at a small negative pressure just sufficient to remove all of the flowing gas. An adjustable wall with an optical window (transparent to both UV and visible lasers) is located inside the downstream end of the test section, to reflect the first shock and study the effects of subsequent reflected shock, henceforth referred to as reshock. The reshock event deposits extra energy in the mixing region, causing faster material mixing. This wall is removed from the test section when conducting single shock experiments.

The imaging of the initial conditions and the ensuing structures after shock and reshock are done using high resolution 2-D particle image velocimetry (PIV) and planar laser-induced fluorescence (PLIF) diagnostics as illustrated by Figure 1(b). The output beams from dual-head, frequency-quadrupled and frequency doubled Nd:YAG lasers operating at a wavelengths of 266 nm and 532 nm are used for PLIF and PIV measurements, respectively. Both laser beams are shaped as thin light sheets of thickness ≤ 1.2 mm. All measurements were done at a plane 20 mm below the nozzle exit. The SF_6 gas is uniformly mixed with acetone vapor for PLIF measurements. The acetone vapor is generated by bubbling SF_6 through a liquid acetone bath maintained at a constant temperature of 20°C using a regulated water bath. The light from the PLIF laser is used to induce fluorescence of the acetone present in the SF_6 . The evolving flow fields after first shock and reshock are captured using an Alta U-42 camera with a 1024×1024 charge coupled device (CCD) array operated with 2×2 on-chip binning and an Apogee 32ME camera with a 2184×1470 CCD array and operating with 3×3 on-chip binning. The PLIF resolution for the Alta U-42 camera is $50.5 \mu\text{m}/\text{pixel}$ and for Apogee camera is $52 \mu\text{m}/\text{pixel}$. Quantitative intensity calibration of the PLIF images is performed using a calibration test cell. The calibration process is done before and after the experiments, in

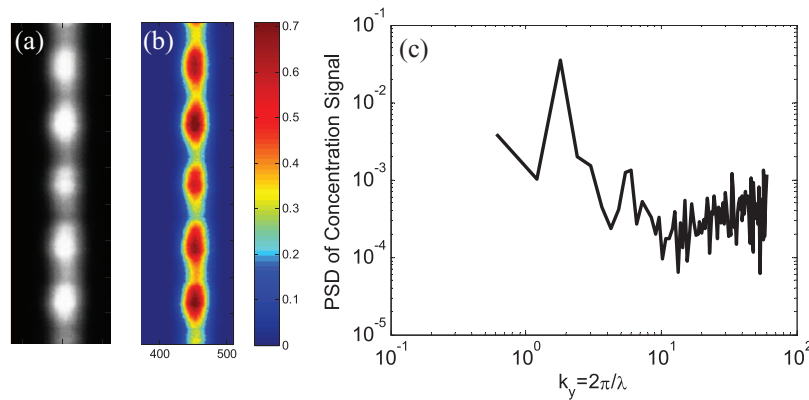


FIG. 2. (a) A PLIF image of varicose initial conditions with primary amplitude $\delta_0 = 3$ mm and wavelength $\lambda_0 = 3.6$ mm. (b) Contour image of the initial conditions showing the relative concentration field of SF₆ at a plane 20 mm below the nozzle exit. (c) Power spectral density of the concentration field of initial condition profile.

order to calculate the concentration of SF₆ at the nozzle exit. This concentration value is used as a baseline for the calculating concentration at different times using conservation of mass within the measurement plane.

For PIV measurements, the flow is uniformly seeded with glycol particles (mixed with SF₆ using a fog machine placed in the settling chamber) and the light scattered off these particles is imaged by a Kodak Megaplus-ES camera with a 2048 × 2048 CCD array. The background fluorescence due to the acetone seeding is removed by using a Raman notch filter, centered at 532 nm with a full width half maximum = 17 nm, attached to the front end of the lens. The PIV vectors are obtained by cross correlating the raw images using INSIGHT 3G. A correlation window size of 32 × 32 pixels is used with suitable offsets for interrogations. A 50% overlap of the windows and a Gaussian smoothing over a 3 × 3 neighborhood of the interrogated field are employed to increase the spatial resolution of the measurement, and to reduce the amount of bad vectors. The PIV spatial resolution is 16.5 μm/pixel, and the vector to vector spacing is 264 μm. For the PIV images, we have approximately 15 glycol particles per interrogation region, ensuring accurate cross-correlation results.²³

Due to the sensitive nature of the flow, it is important to characterize the concentration and velocity field of the varicose gas curtain initial conditions using PLIF and PIV measurements. A contour plot along with an image from the PLIF diagnostic of our experimental initial conditions at the 20 mm plane is shown in Figure 2. This image was obtained after correcting for laser intensity variations in the spanwise (y) direction, and subtracting the background noise due to the surroundings. As seen from this image, the peak concentration of SF₆ at the measurement location is $\approx 60\% \pm 5\%$ with $\approx 20\% \pm 5\%$ acetone, and $\approx 20\% \pm 5\%$ air. The diffusion occurring between successive holes gives a gaussian profile in the streamwise (x) direction and a sinusoidal profile in the spanwise (y) direction.^{20,24} The vertical (z) velocity profiles at different planes of the varicose gas curtain, obtained using PIV, are shown in Figure 3. The inlet velocity profile close to the exit of the nozzle is parabolic, and flattens out as the gas flows down. Also, at the potential core of the jet, the velocity is expected to be maximum (≈ 100 cm s⁻¹ at the measurement plane). From the concentration and velocity measurements, a 3D numerical simulation of our experimental initial conditions can be performed.

The power spectrum of the concentration field for the experimental initial conditions taken along a line at the center of mass of the structure is shown in Figure 2(c). The power spectral density (PSD) from multiple experiments was compared and it was found that the PSD is reproducible over many length-scales. Hence, for clarity the PSD plot shown in Figure 2(c) is from a single experiment. The primary wavenumber, $\kappa_0 = 1.745$ is distinctly seen, with small-scale noise overriding this dominant single mode. We observe from this figure that, the primary mode $\kappa_0 = 1.745$ is ≈ 10 times bigger than the next largest low wavenumber mode $\kappa = 0.62$, and ≈ 30 times bigger than the next largest

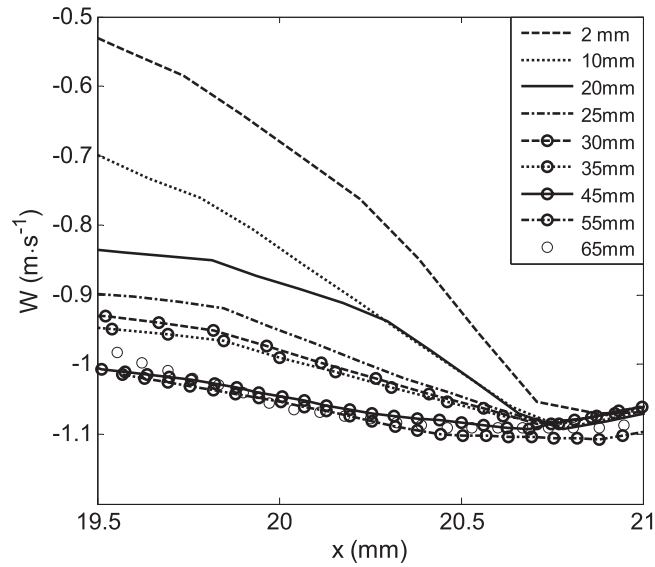


FIG. 3. Vertical (z direction) velocity profiles at different planes of the flowing varicose nozzle initial conditions.

high wavenumber mode $\kappa = 5.35$, thus making it the dominant mode. The small-scale fluctuations in the form of random noise present in the laboratory experiments are captured using the power spectrum. This can be used to determine the amount and magnitude of noise (both long wavelength and short wavelength noise) needed for accurate computational modeling of our initial conditions. This noise is mostly attributed to the random fluctuations present in our experiments, making the initial conditions slightly asymmetric, and thus should be modeled for accurate comparisons. Note that all the measurements except for that shown in Figure 3 were made at a plane $z = 20$ mm below the nozzle exit. It should also be noted that in this study, the effect of glycol droplets on Atwood number was ignored based on the result from previous experimental and numerical studies,^{25,26} that acetone has a much greater influence on the Atwood number and on the evolution of R-M instability.

III. RESULTS AND DISCUSSION

When the varicose gas curtain described in Sec. II is shocked by a Mach $M = 1.2$ shock wave, the interface evolves as shown in Figure 4. The flow development in these experiments was highly

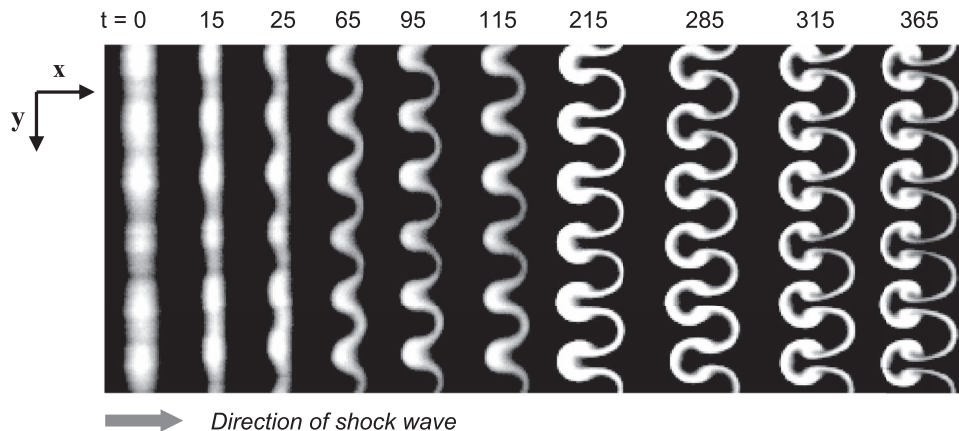


FIG. 4. Time evolution of Richtmyer-Meshkov instability after first shock. White region indicates the heavy fluid, SF₆, while black region indicates the lighter fluid, air. All the times shown are in μs .

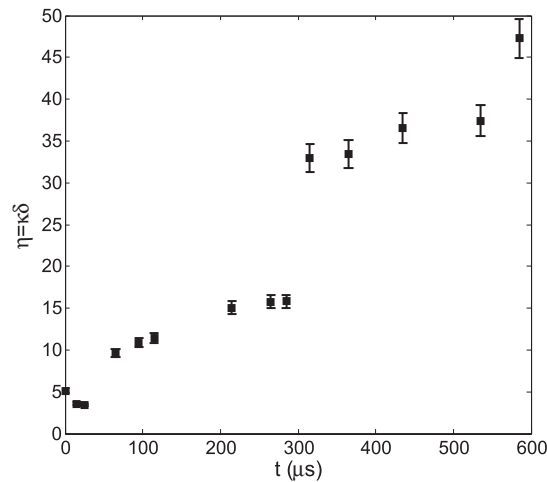


FIG. 5. The growth of dimensionless length-scale, η , after a single shock for R-M instability. As the structures become more complex the value of η increases. The error bars corresponding to 1σ are shown.

reproducible due to the stable nature of initial conditions,²⁰ unlike those reported in Rightley *et al.*²⁷ In Figure 4, time $t = 0 \mu\text{s}$ is the time just before the shock wave interacts with the upstream side of the flowing gas curtain defined at 5% of the peak value of SF_6 concentration. We then reshock the evolving interface at different times. To quantify the differences between the varying reshocked structures, a metric called dimensionless length-scale, η is defined as^{28,29}

$$\eta = \kappa \delta = \left(\sqrt{\frac{\nabla \rho' \nabla \rho'}{\rho' \rho'}} \right) \delta = \frac{\pi N_{zc}}{L_y} \delta, \quad (1)$$

where δ is the amplitude of mixing layer, defined as the difference between the farthest edges of the curtain where the SF_6 concentration reaches $\approx 5\%$ of its maximum value, κ is the zero-crossing wavenumber which is an indicator of the spectral frequency modes present within the interface, ρ' is the density fluctuations, N_{zc} is the number of zero crossings, and L_y is the domain length. The value of κ is experimentally measured by calculating the number of times the interface crosses the zero value (equivalent to sign changes of mass density fluctuation) over a spanwise length (L_y) at a line going through the center of mass. The dimensionless length-scale, η , can also be construed as a measure of the *rms* slope of an interface; thus, the higher the value of η , the more complex the interface. A plot of the evolution of η after first shock is shown in Figure 5. The increasing value of η with time is evident from this figure. However, it is interesting to observe that there is a rapid increase in the value of η at time $t = 315 \mu\text{s}$, when the structures are starting to roll up, forming a mushroom shape. The development of this mushroom shaped morphology enhances the presence of small-scale structures in the flow and thus significantly increases the value of κ and hence η . Another such discontinuity in the value of η is observed at time $t = 585 \mu\text{s}$, where the R-M instability has a more complex shape.²⁰ Experiments were performed by reshocking the evolving structures at varying times, thereby changing both δ and κ of the initial conditions simultaneously.

In the present study three different reshock experiments were conducted at reshock times, denoted as t_{RS} , with corresponding value of η , as follows: (a) $t_{\text{RS}} = 90 \mu\text{s}$, $\eta = 12$, (b) $t_{\text{RS}} = 170 \mu\text{s}$, $\eta = 15$, and (c) $t_{\text{RS}} = 385 \mu\text{s}$, $\eta = 35$. The evolution of the concentration fields obtained using PLIF for these experiments is shown in Figure 6. As seen from the three cases in Figure 6, reshocking an interface with an initially high value of η (representing steeper density gradients) causes the late-time structures to mix and transition to smaller scales at a faster rate, compared to reshocking a structure with low/moderate value of η . To quantitatively measure the visible mixing behaviors for these experiments, the power spectrum along a line at the center of mass of the late-time structures is shown in Figure 7 for the three different reshock times. The time after reshock is $t^* = 210 \mu\text{s}$, where $t^* = t - t_{\text{RS}}$ is the time after the reshock wave has hit the interface. For lower/moderate values of η

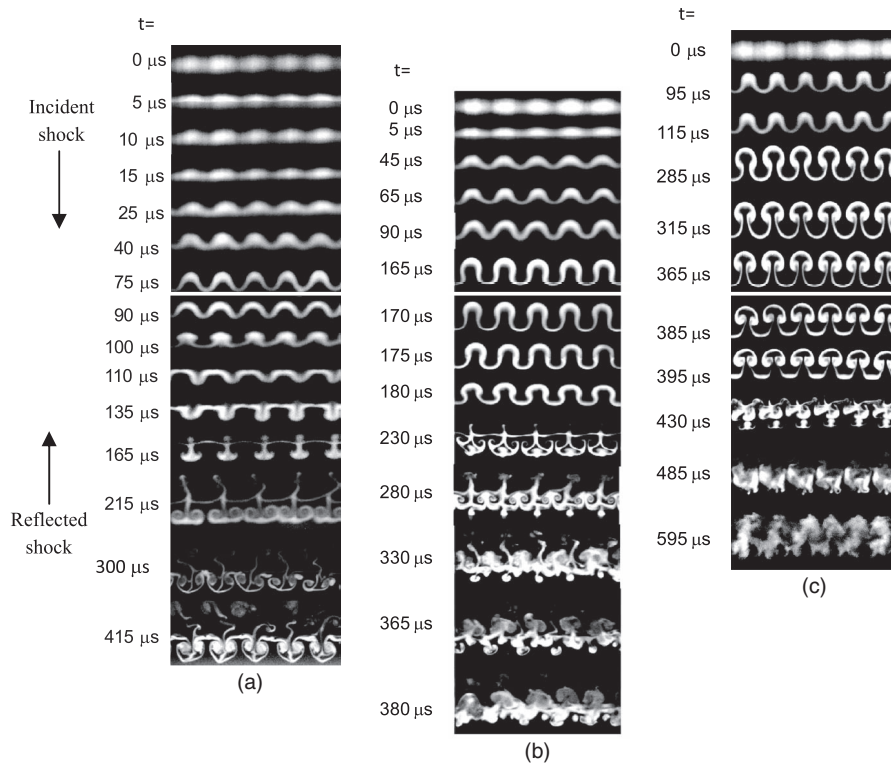


FIG. 6. Three different sets of experiments, each beginning with the varicose gas curtain (top), shocked with a Mach $M = 1.2$ shock that travels downward. Each experiment is then reshocked at a different time, as indicated below the white bar crossing the time series. Reshock occurs at time, $t = t_{RS}$ = (a) $90 \mu\text{s}$, (b) $170 \mu\text{s}$, and (c) $385 \mu\text{s}$. At late times after reshock, approximately $t^* = 210 \mu\text{s}$, the large variation in mixing that occurs for each of the three cases is visible.

(corresponding to an early reshocked interface at $t_{RS} = 90 \mu\text{s}/170 \mu\text{s}$), the dominant wavelength is preserved with some small length-scales, and a transition to a well-mixed state is not evident. On the other hand, for the higher value of η , corresponding to a more complex interface at $t_{RS} = 385 \mu\text{s}$, the spectrum has lost significant features at the primary wavelength, showing more smaller scales, which is also reflected in the post reshock structures from Figure 6 that show a well-mixed state. Due to the enhanced mixing observed in the reshock experiment at $t_{RS} = 385 \mu\text{s}$, additional experiments were

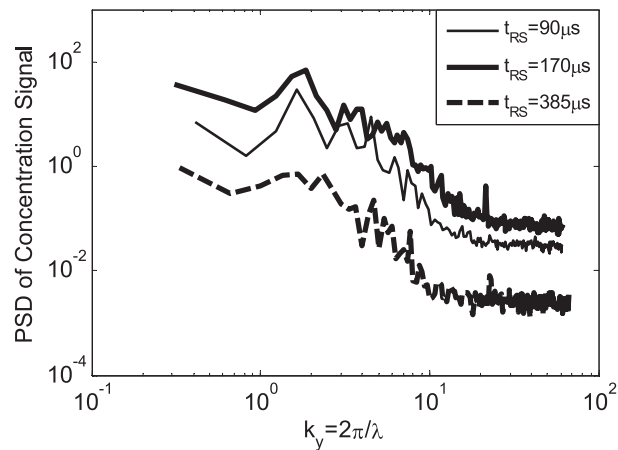


FIG. 7. Power spectral density of the concentration signal for late-time flow structure after reshock at $t^* = 210 \mu\text{s}$ for three different reshock experiments.

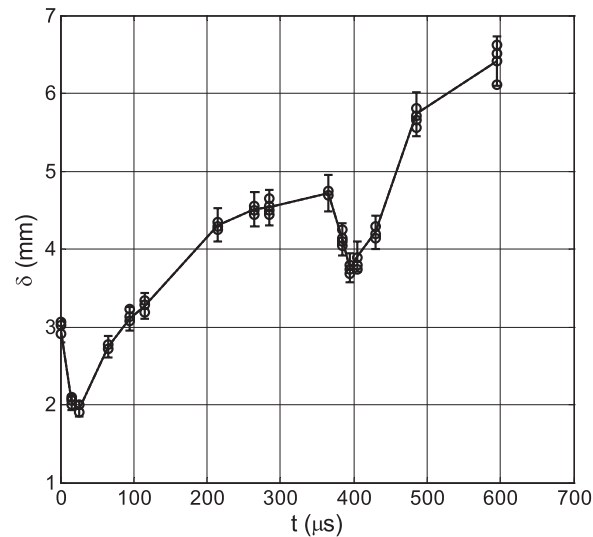


FIG. 8. Plot of amplitude of mixing layer (δ , mm) with time (t , μs) after first shock and reshock at $t = 385 \mu\text{s}$. Open circles represent measurements from several experimental realization. The solid line represents the mean value. The error bars corresponding to 1σ are shown.

conducted at this reshock time to obtain late-time statistics to confirm the well-mixed, transitional nature of the R-M instability.

Before discussing further results for $t_{\text{RS}} = 385 \mu\text{s}$, we present a brief analysis of experimental uncertainties and measurement errors. The sources of error in our experiments are from laser intensity fluctuations that directly affect the amplitude of mixing layer and density measurements, PIV processing method (e.g., size of interrogation window, correlation algorithm) that affects the velocity statistics, sampling errors, and other random errors. The error and accuracy of the results presented below were quantified to the extent possible. The measurement of amplitude of mixing layer from several realizations, after accounting for laser variations in the illumination intensity, is estimated to be accurate to within $\pm 5\%$. Our mean and fluctuation components of velocity measurements obtained using PIV are accurate to within $\pm 3\%$ – 5% . The mean and fluctuating density measurements (and hence density self-correlation, b , see definition below) have higher statistical error, approximately $\pm 10\%$ – 15% .

The amplitude of mixing layer, denoted as δ , was measured as a function of time after first shock and reshock and is shown in Figure 8. After the first shock δ increases rapidly before starting to plateau. Reshock compresses the curtain and puts additional energy into the flow in the form of baroclinic vorticity deposition, resulting in higher value of δ . The amplitude of mixing layer is a good parameter for understanding the large-scales in the flow, and it can be used as a starting metric to match the experimental results with numerical and computational simulations. However, it is necessary to resolve the smaller scales present in the flow to provide more information on mixing. This is achieved using high resolution simultaneous PIV-PLIF measurements made at $t^* = 210 \mu\text{s}$ (real time $t = t^* + t_{\text{RS}} = 595 \mu\text{s}$) that provide velocity and density statistics. Simultaneous PIV-PLIF is a very useful tool for measuring multi-point turbulent statistics in variable density flows, and velocity and density fields can be measured within reasonable error limits. As seen from Figure 9, the power spectra of velocity and density capture the large-scale flow features very well, and most of the differences in the spectra arise when the flow is transitioning to much smaller scales. Here, we use the unique capability of simultaneous PIV-PLIF to measure density and velocity statistics to quantify mixing in shock-accelerated flows with R-M unstable fluid layer.

When compared to some canonical turbulent flows whose statistics are known to be insensitive to minor variations in the initial conditions, the turbulence statistics in a shock-accelerated flow are known to be sensitive to small changes in initial perturbations.^{7,15,17} With the present gas shock tube experimental set-up, we are able to conduct highly repeatable experiments with stable

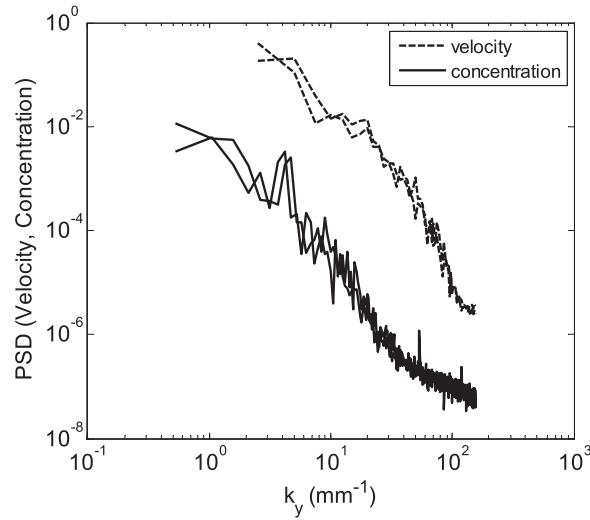


FIG. 9. Power spectral density plot of concentration and velocity at $t = 595 \mu\text{s}$ for the case of reshock at $t_{\text{RS}} = 385 \mu\text{s}$.

membrane-free initial conditions.^{19,20} For the reshock experiment with $t_{\text{RS}} = 385 \mu\text{s}$, to calculate turbulence statistics, we collect ensemble averages by using instantaneous realizations from several runs of the same experiment. The variations between the runs can introduce spurious increases in the calculated turbulence intensities and therefore it is important to measure and document the variations between the individual realizations. Ninety experimental realizations were initially obtained in order to ensure accuracy of the ensemble averaged data. Several criteria were applied to down-select the experiments used in the averaging process as follows: The selected data were required to have variations in shock speed (U , m s^{-1}) within $\pm 0.25\%$, amplitude of mixing layer (δ , mm) within $\pm 5\%$ and the convection velocity (u , m s^{-1}) within $\pm 1\%$. The late-time flow field at $t^* = 210 \mu\text{s}$ after reshock was visually compared to make sure that there were no spurious perturbations to the curtain. Using these criteria, a set of $n = 20$ ensembles (from original ninety ensembles) were processed to obtain reliable velocity and density statistics.

Density self-correlation, b , can be used as a metric to quantify the amount of mixing in variable density flows. During the mixing process, b plays an important role in mediating the mass transport by appearing as an unclosed term in the evolution equation for mass transport.³⁰ The parameter b is defined either in terms of density fluctuation or mean density as shown in Eqs. (3) and (4),

$$\rho'(x, y) = \rho(x, y) - \overline{\rho(x, y)}^n, \quad (2)$$

$$b(x) = -\overline{\rho'(x, y) \left(\frac{1}{\rho(x, y)} \right)^{ny}}, \quad (3)$$

$$b(x) = \left[\overline{\rho(x, y)^{-ny} \left(\frac{1}{\rho(x, y)} \right)^{ny}} \right] - 1. \quad (4)$$

Here, the superscript $-n$ represents ensemble mean of $n = 20$ samples, and the superscript $-ny$ denotes averaging in the spanwise (y) direction of the ensemble mean, thus representing a row averaged quantity. By definition, b is non-negative and equals zero when two fluids are fully mixed in a variable-density flow. From the ensemble data collected in our present experiments, the density self-correlation can be calculated to quantify the amount of mixing.

The shock interaction and compression process changes the density fluctuations within the interface, which in turn changes the value of b . Physically, in variable density flows, at late times, a high value of b means that the interface is less mixed and a low value of b indicates a well mixed state. In Figure 10, the differences in mixing for two times, namely, $t = 285 \mu\text{s}$ (before reshock) and

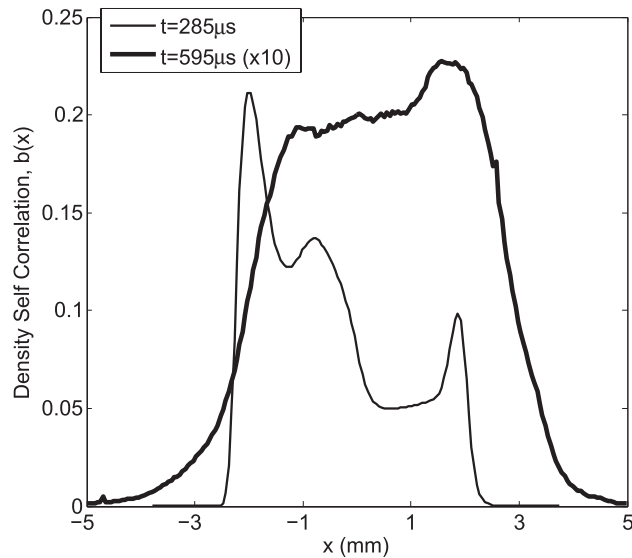


FIG. 10. Plot of density self-correlation, b , indicating the amount of mixing for morphologies formed after first shock and reshock for experiment with $t_{RS} = 385 \mu s$.

$t = 595 \mu s$ (after reshock) for the experiment with $t_{RS} = 385 \mu s$ are shown. The reshock deposits additional energy (and hence vorticity) into the mixing region thereby quickly transitioning to a more mixed and turbulent state, resulting in a very low value of b at $t = 595 \mu s$ (which is ten times less than the early time b value) as seen in the figure. In both cases the peak value of b occurs on the upstream side of the curtain that is first struck by the shock. For the first shock, it is to the left of the center of mass in Figure 10, and for reshock, it is to the right. From Figure 10, the double-peak nature of b is attributed to the fact that the interface is a gas curtain (light-heavy-light). A comparison of b after reshock at time $t^* = 210 \mu s$ for two different reshock experiments at $t_{RS} = 170 \mu s$ and $t_{RS} = 385 \mu s$ with moderate and high values of η is shown in Figure 11. For the case with moderate value of $\eta = 15$, the periodicity and large-scale structures of the flow are preserved. In the case

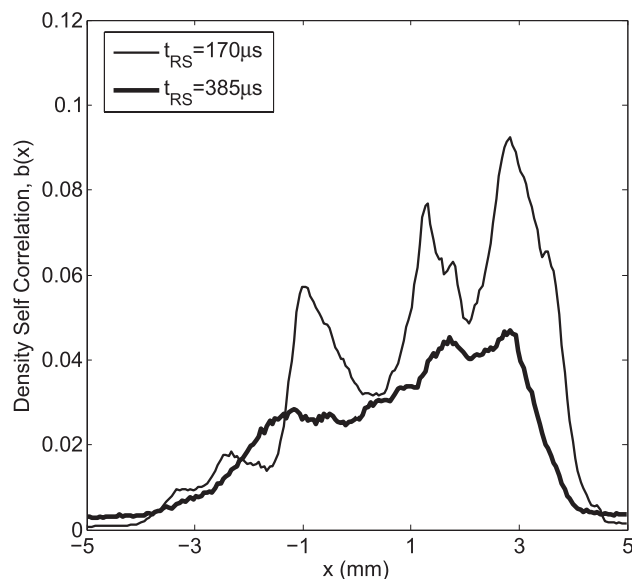


FIG. 11. Plot of density self-correlation, b , indicating the amount of mixing for late-time turbulent structures obtained at time $t^* = 210 \mu s$ for two different reshock times $t_{RS} = 170 \mu s$ and $t_{RS} = 385 \mu s$.

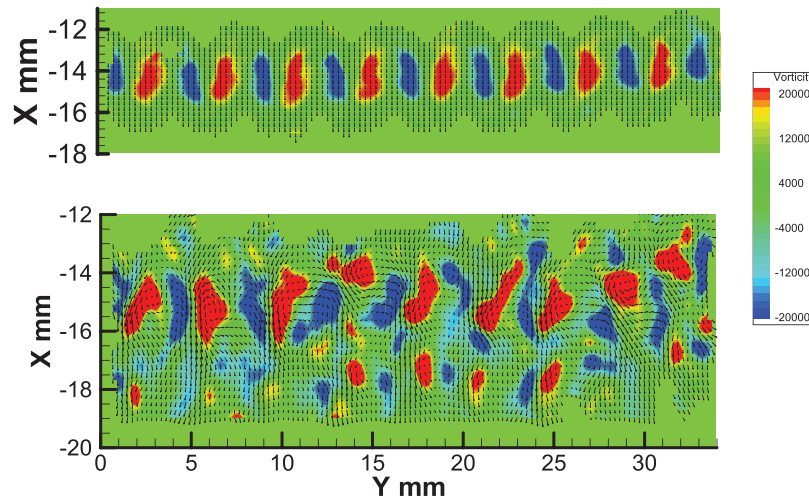


FIG. 12. Contour of vorticity at $t = 365 \mu\text{s}$ and $t = 595 \mu\text{s}$ for reshock at $t_{\text{RS}} = 385 \mu\text{s}$ from Figure 6(c).

of $\eta = 35$, where the flow appears to be more mixed, evidenced by a value of b lower than the $\eta = 15$ case.

The contour plots of the vorticity component, ω_z , across the fluid layer at time $t = 365 \mu\text{s}$ (interface before reshock) and $t = 595 \mu\text{s}$ (interface after reshock) for the experiments of Figure 6(c) reshocked at $t_{\text{RS}} = 385 \mu\text{s}$ are shown in Figure 12. The vorticity field has become disordered due to the breaking down of vortices and transfer of energy from larger scale to smaller scales after reshock. Since the vorticity deposition is the main source of R-M instability production, the breaking down of paired vortices into smaller scales suggests that the flow is transitioning towards a well-mixed turbulent state. The *rms* of the streamwise and spanwise velocity fluctuations across the fluid layer for $t = 595 \mu\text{s}$ is shown in Figure 13. The *rms* of the velocity fluctuation is calculated as the spanwise average of ensemble statistics and is given as

$$u'(x, y) = u(x, y) - \overline{u(x, y)}^n, \quad (5)$$

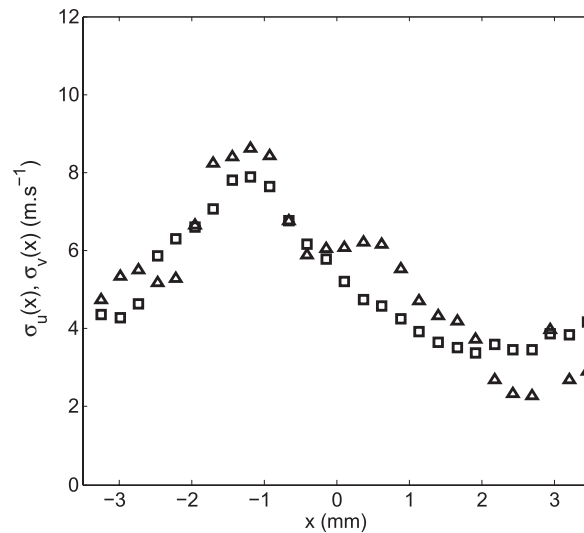


FIG. 13. The *rms* of streamwise (σ_u , Δ) and spanwise (σ_v , \square) velocity fluctuations at $t = 595 \mu\text{s}$ for reshock at $t_{\text{RS}} = 385 \mu\text{s}$.

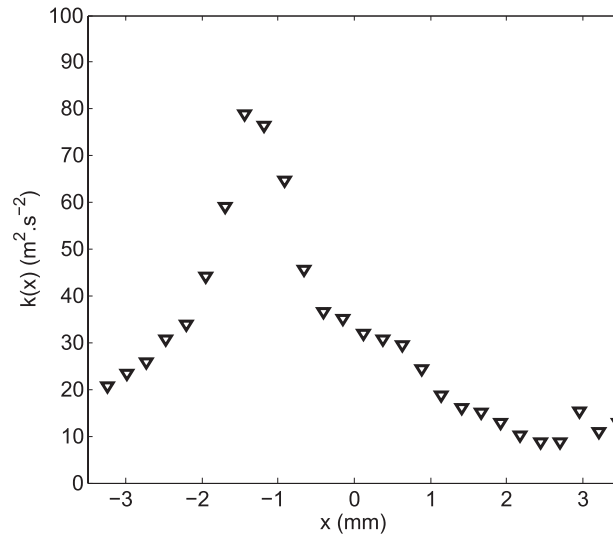


FIG. 14. The turbulent kinetic energy at one instance for interface development at $t = 595 \mu\text{s}$ with reshock occurring at $t = 385 \mu\text{s}$.

$$v'(x, y) = v(x, y) - \overline{v(x, y)^n}, \quad (6)$$

$$\sigma_u(x) = \sqrt{\overline{u'^2(x, y)^{ny}}}, \quad (7)$$

$$\sigma_v(x) = \sqrt{\overline{v'^2(x, y)^{ny}}}. \quad (8)$$

The *rms* of streamwise (i.e., shock direction) velocity, σ_u , and spanwise (i.e., normal to the shock direction) velocity, σ_v are approximately equal in magnitude with similar profiles throughout the fluid layer, indicating that any anisotropy created along the direction of shock propagation in the velocity fields is less than the statistical measurement error. The cross-correlation component denoted as $\overline{u'v'}$, related to the generalized Reynolds shear stress, was found to be smaller than the streamwise and spanwise velocity fluctuations by more than an order of magnitude throughout the fluid layer. This behavior is typical of a well-mixed fluid layer that is homogeneous in the spanwise direction, since a given streamwise velocity fluctuation is equally likely to produce a spanwise fluctuation in either direction. The velocity fluctuations in the z -direction are needed for a complete understanding of the nature of turbulence in the fluid layer, and this is the scope of future work.

The spanwise-averaged 2-D turbulent kinetic energy (k) given by Eq. (9) was calculated across the fluid interface and is shown in Figure 14,

$$k(x) = \frac{1}{2}(\overline{u'^2(x, y)^{ny}} + \overline{v'^2(x, y)^{ny}}). \quad (9)$$

The value of turbulent kinetic energy is highest near the upstream edge of the center of mass, where the deposition of vorticity is maximum (see Figure 12) and b is minimum (see Figure 11), indicating a more mixed region. After this peak, the value of k decreases across the mixing layer in contrast to b , which increases thereby indicating a less mixed region. The asymmetric behavior of k across the fluid layer in the shock direction shows that the mixing layer is non-Boussinesq. The peak values of k , σ_u , and σ_v occur on the upstream side of the mixing layer, indicating turbulence asymmetry in these kind of flows. The turbulent Reynolds number defined as $Re_k = \frac{\sqrt{k}\delta}{\nu} = 8000$ (Taylor Reynolds number, $Re_\lambda = 230$) at time $t = 595 \mu\text{s}$.

The observations of the density field, from Figure 6, show an evolution of mixing from large to small-scales, however, unlike canonical turbulent flows, shock-accelerated flow remain highly

anisotropic. The measurements of b , σ_u and σ_v , and k show that the mixing layer is indeed anisotropic. Also, the power spectra of density field indicate that the flow retains memory of the initial conditions. More work still needs to be done to quantitatively explain the effects of initial conditions and the nature of turbulent mixing for shock-accelerated flows based on the time evolution of production, transport, and dissipation of turbulent kinetic energy (k) and density self-correlation (b).³⁰ We believe that the present results will be useful for numerical and theoretical modeling of such complex flows.

IV. SUMMARY AND CONCLUSIONS

The study of dependence of amplitude, δ and wavenumber, κ of initial perturbations on mixing in shock-accelerated, Richtmyer-Meshkov unstable fluid layer was done experimentally and verified theoretically. A varicose light-heavy-light gas curtain was used to create membrane-free initial conditions, whose initial density and velocity fields were characterized using PLIF and PIV diagnostics. Such a characterization will be useful for initializing 3D numerical simulations of our experimental initial conditions. To understand the effect of multi-mode initial conditions, the evolving interface after the incident shock ($M = 1.2$) were reshocked at various times, thus allowing us to change the δ and κ of perturbations simultaneously. A dimensionless length-scale, $\eta = \kappa\delta$, measuring the *rms* slope of the initial interface, was used to show the dependence of δ and κ on late-time mixing and transition to turbulence. A total of three different experiments were conducted by reshocking varying morphologies with low, moderate, and high values of η . It was observed experimentally that high wavenumber modes quickly enhance the mixing and transition to turbulence in such flows. For the case of high η , various mixing and turbulence statistics such as the width of mixing layer (δ), density self-correlation (b), turbulent kinetic energy (k), and *rms* of the velocity fluctuations (σ_u and σ_v) were measured to quantify the nature of the flow. Initial conditions with a higher value of non-dimensional length-scale η can achieve turbulent mixing faster. Moreover, evidence of the imprint of initial conditions on late-time mixing was qualitatively confirmed in these experiments.

ACKNOWLEDGMENTS

This work is supported by Los Alamos Laboratory Directed Research and Development Program through Directed Research (LDRD-DR). Authors would like to thank the collaborators J. R. Ristorcelli, A. A. Gowardhan, F. F. Grinstein, M. J. Andrews, R. A. Gore, and D. Livescu for useful insights and discussions towards this research. The help rendered by Gavin R. Friedman, a former post baccalaureate student on our team, during data acquisition is gratefully acknowledged.

- ¹ R. D. Richtmyer, "Taylor instability in shock acceleration of compressible fluids," *Commun. Pure Appl. Math.* **13**, 297 (1960).
- ² E. E. Meshkov, "Instability of the interface of two gases accelerated by a shock wave," *Fluid Dyn.* **4**, 101 (1969).
- ³ P. Amendt, O. L. Landen, H. F. Robey, C. K. Li, and R. D. Petrasso, "Plasma barodiffusion in inertial-confinement-fusion implosions: Application to observed yield anomalies in thermonuclear fuel mixtures," *Phys. Rev. Lett.* **105**, 115005 (2010).
- ⁴ J. D. Lindl, R. L. McCrory, and E. M. Campbell, "Progress toward ignition and burn propagation in inertial confinement fusion," *Phys. Today* **45**(9), 32 (1992).
- ⁵ D. L. Youngs, "Numerical simulation of turbulent mixing by Rayleigh-Taylor instability," *Physica D* **12**, 32 (1984).
- ⁶ D. Oron, L. Arazi, D. Kartoon, A. Rikanati, U. Alon, and D. Shvarts, "Dimensionality dependence of the Rayleigh-Taylor and Richtmyer-Meshkov instability late-time scaling laws," *Plasma Phys.* **8**, 2883 (2001).
- ⁷ W. K. George, "Recent advancements toward the understanding of turbulent boundary layers," *AIAA J.* **44**, 2435 (2006).
- ⁸ G. Dimonte *et al.*, "A comparative study of the turbulent Rayleigh-Taylor instability using high-resolution three-dimensional numerical simulations: The Alpha-Group collaboration," *Phys. Fluids* **16**(5), 1668 (2004).
- ⁹ P. Ramaprabhu, G. Dimonte, and M. J. Andrews, "A numerical study of the influence of initial perturbations on the turbulent Rayleigh-Taylor instability," *J. Fluid Mech.* **536**, 285 (2005).
- ¹⁰ A. Banerjee, and M. J. Andrews, "3-D Simulations to investigate initial condition effects on the growth of Rayleigh-Taylor mixing," *Int. J. Heat Mass Transfer* **52**, 3906 (2009).
- ¹¹ Y. Yang, Q. Zhang, and D. H. Sharp, "Small amplitude theory of Richtmyer-Meshkov instability," *Phys. Fluids* **6**, 1856 (1994).
- ¹² P. G. Saffman and D. I. Meiron, "Kinetic energy generated by the incompressible Richtmyer-Meshkov instability in a continuously stratified fluid," *Phys. Fluids A* **1**, 1767 (1989).
- ¹³ M. Brouillette and B. Sturtevant, "Experiments on the Richtmyer-Meshkov instability: small-scale perturbations on a plane interface," *Phys. Fluids A* **5**, 916 (1993).

- ¹⁴D. J. Hill, C. Pantano, and D. I. Pullin, "Large-eddy simulation and multiscale modelling of a Richtmyer-Meshkov instability with reshock," *J. Fluid Mech.* **557**, 29 (2006).
- ¹⁵B. Thornber, D. Drikakis, D. L. Youngs, and R. J. R. Williams, "The influence of initial conditions on turbulent mixing due to Richtmyer-Meshkov instability," *J. Fluid Mech.* **654**, 99 (2010).
- ¹⁶A. R. Miles, M. J. Edwards, and J. A. Greenough, "Effects of initial conditions on compressible mixing in supernova-relevant laboratory experiments," *Astrophys. Space Sci.* **298**, 17 (2005).
- ¹⁷M. Hahn, D. Drikakis, D. L. Youngs, and R. J. R. Williams, "Richtmyer-Meshkov turbulent mixing arising from an inclined material interface with realistic surface perturbations and reshocked flow," *Phys. Fluids* **23**, 4 (2011).
- ¹⁸J. K. Prasad, A. Rasheed, S. Kumar, and B. Sturtevant, "The late-time development of the Richtmyer-Meshkov instability," *Phys. Fluids* **12**, 2108 (2000).
- ¹⁹B. J. Balakumar, G. C. Orlicz, C. D. Tomkins, and K. P. Prestridge, "Dependence of growth patterns and mixing width on initial conditions in Richtmyer-Meshkov unstable fluid layers," *Phys. Scr.* **132**, 014013 (2008).
- ²⁰B. J. Balakumar, G. C. Orlicz, C. D. Tomkins, and K. P. Prestridge, "Simultaneous particle-image velocimetry-planar laser-induced fluorescence measurements of Richtmyer-Meshkov instability growth in a gas curtain with and without reshock," *Phys. Fluids* **20**, 124103 (2008).
- ²¹J. W. Jacobs and J. M. Sheeley, "Experimental study of incompressible Richtmyer-Meshkov instability," *Phys. Fluids* **8**, 405 (1996).
- ²²E. Leinov, G. Malamud, Y. Elbaz, L. A. Levin, G. Ben-Dor, D. Shvarts, and O. Sadot, "Experimental and numerical investigation of the Richtmyer-Meshkov instability under reshock conditions," *J. Fluid Mech.* **626**, 449 (2009).
- ²³R. J. Adrian, "Dynamic ranges of velocity and spatial resolution of particle image velocimetry," *Meas. Sci. Technol.* **8**, 1393 (1997).
- ²⁴K. O. Mikaelian, "Numerical simulations of Richtmyer-Meshkov instabilities in finite-thickness fluids layers," *Phys. Fluids* **8**, 1269 (1996).
- ²⁵C. Tomkins, S. Kumar, G. Orlicz, and K. Prestridge, "An experimental investigation of mixing mechanisms in shock-accelerated flow," *J. Fluid Mech.* **611**, 131 (2008).
- ²⁶S. K. Shankar, S. Kawai, and Sanjiva K. Lele, "Two-dimensional viscous flow simulation of a shock accelerated heavy gas cylinder," *Phys. Fluids* **23**, 2 (2011).
- ²⁷P. M. Rightley, P. Vorobieff, and R. F. Benjamin, "Evolution of shock-accelerated thin fluid layer," *Phys. Fluids* **9**, 1779 (1997).
- ²⁸J. R. Ristorcelli and N. Hjelm, "Initial moments and parameterizing transition for Rayleigh-Taylor unstable stochastic interfaces," *J. Turbul.* **11**, 46 (2010).
- ²⁹A. A. Gowardhan, J. R. Ristorcelli, and F. F. Grinstein, "The bipolar behavior of the Richtmyer-Meshkov instability," *Phys. Fluids* **23**, 7 (2011).
- ³⁰D. Besnard, F. H. Harlow, R. M. Rauenzahn, and C. Zemach, "Turbulence transport equations for variable-density turbulence and their relationship to two-field models," Los Alamos National Laboratory Technical Report No. LA-12303-MS, 1992.